Diverse magnetic quantization in bilayer silicene

Thi-Nga Do,[1] Po-Hsin Shih,[2] Godfrey Gumbs,[3] Danhong Huang,[4] Chih-Wei Chiu,[1] and Ming-Fa Lin[5,6,*]

[1]*Department of Physics, National Kaohsiung Normal University, Kaohsiung, Taiwan 82446, Republic of China*

[2]*Department of Physics, National Cheng Kung University, Tainan, Taiwan 701, Republic of China*

[3]*Department of Physics and Astronomy, Hunter College of the City University of New York, 695 Park Avenue, New York, New York 10065, USA*

[4]*US Air Force Research Laboratory, Space Vehicles Directorate, Kirtland Air Force Base, New Mexico 87117, USA*

[5]*Hierarchical Green-Energy Materials Research Center, National Cheng Kung University, Tainan, Taiwan 701, Republic of China*

[6]*Quantum Topology Center, National Cheng Kung University, Tainan, Taiwan 701, Republic of China*

(Received 30 November 2017; revised manuscript received 11 January 2018; published 14 March 2018)

The generalized tight-binding model is developed to investigate the rich and unique electronic properties of AB-bt (bottom-top) bilayer silicene under uniform perpendicular electric and magnetic fields. The first pair of conduction and valence bands, with an observable energy gap, displays unusual energy dispersions. Each group of conduction/valence Landau levels (LLs) is further classified into four subgroups, i.e., the sublattice- and spin-dominated LL subgroups. The magnetic-field-dependent LL energy spectra exhibit irregular behavior corresponding to the critical points of the band structure. Moreover, the electric field can induce many LL anticrossings. The main features of the LLs are uncovered with many van Hove singularities in the density-of-states and nonuniform delta-function-like peaks in the magnetoabsorption spectra. The feature-rich magnetic quantization directly reflects the geometric symmetries, intralayer and interlayer atomic interactions, spin-orbital couplings, and field effects. The results of this work can be applied to novel designs of Si-based nanoelectronics and nanodevices with enhanced mobilities.

DOI: 10.1103/PhysRevB.97.125416

I. INTRODUCTION

Two-dimensional (2D) materials, such as group-IV and -V layered structures [1–22], have become main-stream condensed-matter systems since the discovery of graphene in 2004 by mechanical exfoliation. They possess unique geometric properties, nanoscaled thicknesses, a specific lattice symmetry, a planar/buckled structure, and a stacking configuration. Such systems are verified/predicted to exhibit diverse physical properties and have many potential device applications. Their Hamiltonians include complex effects from orbital bonding, spin-orbital coupling (SOC), magnetic fields, electric fields, and interlayer atomic interactions. How to solve them becomes one of the basic tasks in solid-state physics today. This work is mainly focused on magnetoelectronic properties of AB-stacked bilayer silicene.

Recently, few-layer silicene with buckled honeycomb lattices have been successfully synthesized on Ag(111), Ir(111), and $ZrBi_2$ surfaces [3,4]. According to first-principles calculations [5–10,12], these buckled structures might be metastable. Both AB and AA stackings, being characterized by the (x,y)-plane projection, display bottom-top (bt) and bottom-bottom (bb) configurations on the (x,z) plane [9]. Up to now, the AB-bt and AB-bb configurations have been confirmed by high-angle annular dark-field scanning transmission electron microscopy [16]. The geometric symmetry, the intralayer and interlayer atomic interactions, and SOC are expected to dominate the low-energy physical properties. For example, monolayer silicene presents a slightly displaced Dirac cone with a narrow direct band gap ($E_g \sim 10$ meV) in the presence of SOC [3]. The low-lying band structures in bilayer silicene becomes very sensitive to changes in stacking configurations, such as the stacking-induced indirect gap in AB-bt and semimetal in AA-bb configurations. The former, with the lowest ground-state energy, is chosen to be a model system in this paper for studying magnetic quantization phenomena.

The low-energy electronic properties of monolayer silicene are mainly determined by the outer $3p_z$ orbitals, similar to graphene systems. The perturbation approximation of the 4×4 Hamiltonian could be made around the high-symmetry point [the **K** point in Fig. 1(a)], and then the magnetic quantization follows in a straightforward way. The LL energies are found to be related to the energy gap and Fermi velocity analytically [23]. These LLs look similar to those of monolayer graphene as their magnitudes become much larger than E_g. It has been noticed that the LLs remain doubly degenerate for the spin degree of freedom even with the SOC [23], and the effective-mass approximation becomes too cumbersome for bilayer silicene with the unusual band structures. On the other hand, the generalized tight-binding model has been developed for solving rigorous Hamiltonians in various condensed-matter systems. It is built on subenvelope functions of distinct sublattices [Fig. 1(d)], in which all the intrinsic interactions and the external fields can be taken into consideration simultaneously [24]. Specifically, the magnetically quantized energy spectra and wave functions could be evaluated very efficiently through the exact diagonalization method even for a very large Hamiltonian matrix with complex elements. This model has been utilized to carry out systematic studies of the

*Author to whom all correspondence should be addressed: mflin@mail.ncku.edu.tw

magnetic properties of graphene-related systems [25,26]. It has been proven suitable for studying the rich magnetic quantization phenomena in bilayer silicene with different stacking configurations as well as complicated interlayer atomic interactions.

In this paper, we use the generalized tight-binding model, accompanied by the dynamic Kubo formula and gradient approximation, to investigate the low-energy electronic and optical properties of AB-bt silicene in the presence of uniform magnetic ($B_z\hat{z}$) and electric ($E_z\hat{z}$) fields. The main features of the quantized LLs, energy spectra, and spatially oscillating modes are thoroughly examined, especially for the composite effects arising from intrinsic interactions and external fields. This work demonstrates that LLs are characterized by the dominating (B^1 and B^2) sublattices and spin configurations, leading to four subgroups of conduction/valence LLs. This LL degeneracy splitting will effectively reduce both the impurity and phonon scatterings and result in enhanced mobilities at the same time. The unique LLs are directly reflected in the magneto-optical conductivities with a lot of single, double, and twin nonuniform δ-function-like peaks. The sublattice- and spin-dependent LL energies are confirmed by the calculated density of states (DOS), for which the B_z-induced energy splitting behaviors could be verified through experiments using scanning tunneling microscopy (STM). Additionally, the LL energies are found to be tuned easily by an electric field, leading to the crossing and anticrossing energy-spectral features that could be selected by the electric field. Therefore, the use of bilayer silicene, in comparison with monolayer silicene and bilayer graphene, has brought about a new opportunity for gate-controlled magnetoquantum channel conductance, which is expected to be very useful for novel designs of Si-based nanoelectronics and nanodevices [27–29].

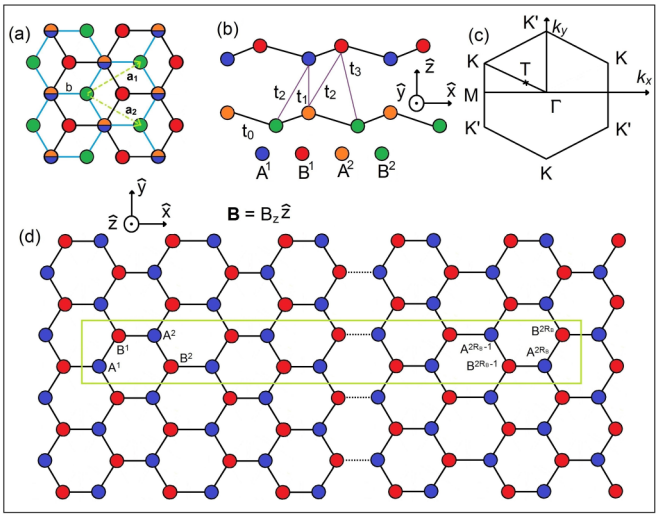

FIG. 1. The top view (a) and side view (b) of the atomic structure for bilayer silicene with intra- and interlayer atomic interactions. The first Brillouin zone along the high-symmetry points is illustrated in (c); the highly symmetric $\mathbf{K}$ ($\mathbf{K}'$) and Γ points and an extreme one, $\mathbf{T}(k_x = 0.1 \times \sqrt{3}, k_y = 0.1)$ (1/Å), are presented. The enlarged rectangular-shaped unit cell under a uniform perpendicular magnetic field is shown in (d).

II. METHOD

The generalized tight-binding model has been developed to investigate the feature-rich electronic properties of AB-bt bilayer silicene arising from intralayer and interlayer atomic interactions, SOC, and the buckled structure. The magnetic and electric fields are simultaneously included in our calculations. The AB-bt bilayer silicene, with the low-buckled honeycomb lattice, consists of four silicon atoms in a unit cell, as depicted in Fig. 1(a). The two primitive unit vectors, $\mathbf{a_1}$ and $\mathbf{a_2}$, have a lattice constant of $a = 3.86$ Å [12]. Bilayer silicene acquires four sublattices of (A^1, B^1) and (A^2, B^2). For each layer, the two sublattices lie on two distinct buckling planes with a separation of $l_z = 0.46$ Å. B^1 and B^2 are located on the higher and lower planes, respectively, for which the interlayer distance is 2.54 Å. The buckled angle due to the intralayer Si-Si bond and the z axis is $\theta = 78.3^\circ$. The low-energy electronic properties are dominated by the silicon $3p_z$ orbitals. The Hamiltonian built from the tight-binding model includes the intra- and interlayer atomic interactions and two kinds of SOCs. The intralayer hopping integral and two kinds of SOCs are similar to monolayer silicene in the previous theoretical prediction [30]. On the other hand, AB-bt bilayer silicene exhibits layer-dependent SOC, a vertical and two nonvertical interlayer atomic interactions, which is absent in monolayer silicene. Such a complicated Hamiltonian could be written as

$$H = \sum_{m,l} (\epsilon_m^l + U_m^l) c_{m\alpha}^{\dagger l} c_{m\alpha}^l + \sum_{m,j,\alpha,l,l'} t_{mj}^{ll'} c_{m\alpha}^{\dagger l} c_{j\alpha}^{l'} + \frac{i}{3\sqrt{3}} \sum_{\langle\langle m,j\rangle\rangle,\alpha,\beta,l} \lambda_l^{\mathrm{SOC}} \gamma_l v_{mj} c_{m\alpha}^{\dagger l} \sigma_{\alpha\beta}^z c_{j\beta}^l - \frac{2i}{3} \sum_{\langle\langle m,j\rangle\rangle,\alpha,\beta,l} \lambda_l^R \gamma_l u_{mj} c_{m\alpha}^{\dagger l} (\vec{\sigma} \times \hat{d}_{mj})_{\alpha\beta}^z c_{j\beta}^l. \quad (1)$$

Here, $\epsilon_m^l(A^l, B^l)$ is the sublattice-dependent site energy related to the chemical environment difference [$\epsilon_m^l(A^l) = 0; \epsilon_m^l(B^l) = -0.12$ eV]. $U_m^l(A^l, B^l)$ is the height-induced Coulomb potential energy arising from a uniform perpendicular electric field. The $c_{m\alpha}^l/c_{m\alpha}^{\dagger l}$ operator represents the annihilation/creation of an electronic state with spin polarization α at the mth site of the lth layer. The atomic interactions in the second term cover the nearest-neighbor intralayer hopping integral ($t_0 = 1.13$ eV) and three interlayer hopping integrals due to (A^1, A^2), (B^1, A^2), or (A^1, B^2) and (B^1, B^2) [$t_1 = -2.2$ eV, $t_2 = 0.1$ eV, and $t_3 = 0.54$ eV in Fig. 1(b)]. Specifically, the large interlayer vertical hopping integral of t_1 induces very strong orbital hybridizations in bilayer silicene. The traditional SOC (the third term) and the Bychkov-Rashba SOC (the fourth term) take into account the next-nearest-neighbor pairs $\langle\langle m, j\rangle\rangle$. $\vec{\sigma}$ is the Pauli spin matrix and $\hat{d}_{mj} = \vec{d}_{mj}/|d_{mj}|$ denotes the unit vector connecting the mth and jth lattice sites. $v_{mj} = \pm 1$ when the next-nearest-neighbor hopping is anticlockwise/clockwise with respect to the positive z axis. $u_{mj} = \pm 1$ corresponds to the A and B sites, respectively. $\gamma_l = \pm 1$ presents the layer-dependent SOCs due to the opposite buckled ordering of AB-bt bilayer silicene. Two kinds of SOCs appear in the diagonal elements of the Hamiltonian matrix. They are chosen

as $\lambda_1^{\mathrm{SOC}} = 0.06$ eV, $\lambda_2^{\mathrm{SOC}} = 0.046$ eV, $\lambda_1^R = -0.054$ eV, and $\lambda_2^R = -0.043$ eV so that the calculated band structure approaches that from the first-principles method [10].

A uniform perpendicular magnetic field can produce an extra Peierls phase in the tight-binding function through the vector potential $\vec{A}$, leading to an enlarged rectangular-shape unit cell, as illustrated in Fig. 1(d). The Peierls phase is characterized by $G_R = \frac{2\pi}{\phi_0}\int_R^r \vec{A}\cdot d\vec{l}$, in which $\phi_0 = hc/e$ is the magnetic flux quantum and $\phi = B_z\sqrt{3}a^2/2$ is the magnetic flux through a hexagon. There are totally $16R_B$ ($R_B = \phi_0/\phi$) Si atoms in the enlarged unit cell. The resulting magnetic Hamiltonian, based on the tight-binding atomic base functions in distinct sublattices, is a $16R_B \times 16R_B$ Hermitian matrix. The eigenvalues and eigenfunctions of the magnetic Hamiltonian are efficiently solved numerically using the bandlike method and the spatial localizations of the magnetic wave functions. After the diagonalization of the bilayer magnetic Hamiltonian, the Landau-level wave function, with quantum number n, could be expressed as

$$\Psi(n,\mathbf{k}) = \sum_{l=1,2}\sum_{m=1}^{R_B}\sum_{\alpha,\beta}\left[A_{\alpha,\beta}^{l,m}(n,\mathbf{k})|\psi_{\alpha,\beta}^{l,m}(A)\rangle + B_{\alpha,\beta}^{l,m}(n,\mathbf{k})|\psi_{\alpha,\beta}^{l,m}(B)\rangle\right]. \quad (2)$$

Here, $\psi_{\alpha,\beta}^{l,m}$ is the tight-binding function localized at the sublattice-dependent lattice sites, and $A_{\alpha,\beta}^{l,m}(n,\mathbf{k})$ [$B_{\alpha,\beta}^{l,m}(n,\mathbf{k})$] is the amplitude on the sublattice-dependent lattice site. Specifically, all the amplitudes in an enlarged unit cell could be regarded as the spatial distributions of the subenvelope functions on the distinct sublattices. This is because the magnetic distribution width is much larger than the lattice constant. Such subenvelope functions provide much information for explaining the interesting LL behaviors, such as the LL quantum number, the localization centers, and the crossing/anticrossing phenomena. For bilayer silicene, the buckled honeycomb structure, the complex intra- and interlayer atomic interactions, and the significant SOCs need to be fully taken into account in the theoretical model calculations. Such a system is expected to show diverse physical properties under various external fields.

The zero-field and magneto-optical conductivities are taken into consideration. The optical conductivity can be expressed as $\sigma(\omega) \propto A(\omega)/\omega$, in which the optical-absorption function, $A(\omega)$, is calculated according to the Fermi golden rule,

$$A(\omega) \propto \sum_{c,v,m,m'}\int_{1\mathrm{stBZ}}\frac{d\mathbf{k}}{(2\pi)^2}\left|\left\langle\Psi^c(\mathbf{k},m')\left|\frac{\hat{\mathbf{E}}\cdot\mathbf{P}}{m_e}\right|\Psi^v(\mathbf{k},m)\right\rangle\right|^2 \times \mathrm{Im}\left[\frac{f(E^c(\mathbf{k},m')) - f(E^v(\mathbf{k},m))}{E^c(\mathbf{k},m') - E^v(\mathbf{k},m) - \omega - i\Gamma}\right]. \quad (3)$$

$\mathbf{P}$ is the momentum operator, $f(E^{c,v}(\mathbf{k},m))$ is the Fermi-Dirac distribution function, and Γ is the broadening parameter. The absorption spectrum is associated with the velocity matrix elements (the first term) and the joint density of states (the second term). The former can determine whether the inter-LL transitions are available. The velocity matrix elements, as successfully done for carbon-related materials [32], are evaluated under the gradient approximation in the form of

$$\left\langle\Psi^c(\mathbf{k},m')\left|\frac{\hat{\mathbf{E}}\cdot\mathbf{P}}{m_e}\right|\Psi^v(\mathbf{k},m)\right\rangle \cong \frac{\partial}{\partial k_y}\langle\Psi^c(\mathbf{k},m')|H|\Psi^v(\mathbf{k},m)\rangle$$
$$= \sum_{l,l'=1}^{3}\sum_{m,m'=1}^{2R_B}\left(c^*_{A^l_{m,\mathbf{k}}}c_{A^{l'}_{m',\mathbf{k}}}\frac{\partial}{\partial k_y}\langle A^l_{m,\mathbf{k}}|H|A^{l'}_{m,\mathbf{k}'}\rangle + c^*_{A^l_{m,\mathbf{k}}}c_{B^{l'}_{m',\mathbf{k}}}\frac{\partial}{\partial k_y}\langle A^l_{m,\mathbf{k}}|H|B^{l'}_{m,\mathbf{k}'}\rangle + c^*_{B^l_{m,\mathbf{k}}}c_{A^{l'}_{m',\mathbf{k}}}\frac{\partial}{\partial k_y}\langle B^l_{m,\mathbf{k}}|H|A^{l'}_{m,\mathbf{k}'}\rangle + c^*_{B^l_{m,\mathbf{k}}}c_{B^{l'}_{m',\mathbf{k}}}\frac{\partial}{\partial k_y}\langle B^l_{m,\mathbf{k}}|H|B^{l'}_{m,\mathbf{k}'}\rangle\right). \quad (4)$$

In this approximation, we do not need to really do the inner product of the left side in Eq. (4); that is, the tight-binding functions of the $2p_z$ orbital are not included in the calculation, but only amplitudes are sufficient on the right-hand side of Eq. (4). This means that the subenvelope functions can be used to calculated the magnetoabsorption spectra. A similar theoretical framework is available in understanding the quantum Hall conductivities. In general, we can fully understand the critical factors purely due to the characteristics of LLs, e.g., monolayer graphene presents many symmetric δ-function-like absorption peaks with uniform intensity in the magnetoabsorption spectrum [33].

In general, there are two kinds of theoretical models to study the magnetic quantization phenomena, namely the low-energy elective-mass approximation and the tight-binding model. Concerning the low-energy perturbation method [34,35], the zero-field Hamiltonian matrix elements are expanded about the high-symmetry points (e.g., the **K** point in graphene). And then, the magnetic quantization is further made from an approximate Hamiltonian matrix. That is to say, the zero-field and magnetic Hamiltonian matrices have the same dimension. However, some interlayer hopping integrals in layered graphene will create much difficulty in the study of magnetic quantization. Some of them are usually ignored in the effective-mass approximation. Consequently, certain unique and diverse magnetic quantization phenomena are lost by using this method, e.g., the anticrossing phenomenon in ABC-stacked trilayer graphene, and the extra magnetoabsorption selection rules [10]. In general, this perturbation method cannot deal with the low-symmetry systems with multiconstant energy loops. For AB-bt bilayer silicene, it may be impossible to solve for the low-lying energy bands with the use of a low-energy expansion method; that is, the effective-mass model is not suitable for expanding the low-energy electronic states from the **K** and **T** points simultaneously. This model becomes too cumbersome to generate the further magnetic quantization. So, it is very difficult to comprehend the LLs, being attributed to the unique Hamiltonian in bilayer silicene. This is in sharp contrast with the monolayer silicene case.

Within the tight-binding method, the magnetic phases due to the vector potential are included in the calculations. In previous studies [36,37], this model was developed using the $\vec{\mathbf{k}}$ scheme, but not the $\vec{\mathbf{r}}$ scheme. That is, the magnetic states were built from the original electronic states in the first

Brillouin zone (the hexagonal Brillouin zone in graphene). However, it is not suitable to present the main features of LL wave functions (oscillatory distribution in real space with localization centers). Explicitly, the subenvelope functions could not be identified as the LL wave functions since they are only random distributions. In this scheme, it is very difficult to deal with the essential properties under a spatially modulated/nonuniform magnetic field, the modulated electric field, and the composite magnetic and electric fields, e.g., the magneto-optical properties and magneto-Coulomb excitations. For the generalized tight-binding model used in this study, the calculations are based on the sublattices in an enlarged unit cell in real space. Under a perpendicular magnetic field, the Hamiltonian matrix becomes huge so that we need to arrange it in a bandlike form. The magnetic Hamiltonian is dependent on k_x and k_y in the reduced first Brillouin zone. Moreover, LL energies are fully degenerate in this Brillouin zone. The LL degeneracy is $D = \frac{\vec{\mathbf{B}}\cdot S_{\rm hex}}{h/2e} \approx \frac{32\,000}{B_z}$. In addition, the original hexagonal first Brillouin zone is changed into a small rectangular one. The degenerate (k_x,k_y) states in the reduced first Brillouin zone only make the same contribution for any physical properties. Therefore, we choose the $(k_x = 0,k_y = 0)$ state to study the magnetoelectronic properties of bilayer silicene.

III. RESULTS AND DISCUSSION

A. Electronic structure

AB-bt bilayer silicene exhibits a feature-rich band structure due to its buckled lattice, complex intra- and interlayer atomic interactions, and significant SOCs. There exist two pairs of conduction and valence bands. This work will mainly address the electronic properties of the low-lying energy bands, as clearly indicated in Fig. 2(a). The conduction and valence bands display an asymmetric energy spectrum about the Fermi level ($E_F = 0$), strong energy dispersions, a highly anisotropic behavior, and a spin-dependent double degeneracy [the spin-up- and spin-down-dominated degenerate states discussed with respect to Figs. 2(b)–2(e)]. The conduction-band valley is initiated from the **K** point and presents a special shoulderlike structure along the **K**-Γ direction in the range $0.2 < E^c < 0.22$ eV. On the other hand, the valence-state valley is built from the **T** point between the **K** and Γ points; furthermore, the unusual energy spectrum, with an extreme **K** point, is revealed along the **TK** direction at $E^v \sim -0.33$ eV. There exists a noticeable indirect gap of 0.3 eV, corresponding to the highest occupied state at the **T** point and the lowest unoccupied state at the **K** point. This is in sharp contrast with the zero-gap band structures of bilayer graphene [31]. These special properties leave footprints in the different magnetoelectronic properties discussed in the next subsection.

The state probabilities on the distinct sublattices, $A^{1,2}$ and $B^{1,2}$ with spin-up and spin-down configurations (↑ and ↓), could provide mutual dependence among them, as clearly presented in Figs. 2(b)–2(e). The doubly degenerate states have identical wave functions under interchange of $(B^1_\uparrow, B^1_\downarrow, A^1_\uparrow, A^1_\downarrow)$ and $(B^2_\downarrow, B^2_\uparrow, A^2_\downarrow, A^2_\uparrow)$, and each one exhibits very strong sublattice, spin, and wave-vector dependence. The conduction states are dominated by the $B^1_\uparrow$ sublattice, especially for the full

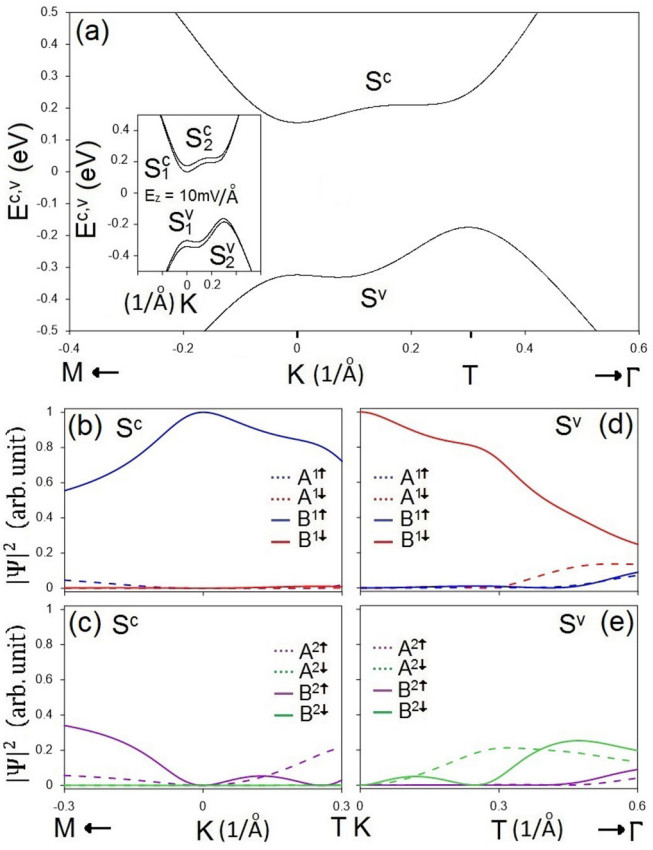

FIG. 2. The first pair of conduction and valence energy bands (a) at $E_z = 0$, the state probabilities for the conduction band (b),(c) and the valence band (d),(e). Also shown in the inset of (a) are E_z-split energy bands.

dominance at the **K** point [see the solid blue curve in Fig. 2(b)]. The $B^2_\uparrow$ sublattice also makes some important contributions to the **K**-valley states [the solid purple curve in Fig. 2(c)]. As for the **T**-valley valence states, the $B^1_\downarrow$ sublattice shows strong dominance [see the red curve in Fig. 2(d)], accompanied by a partial contribution from the $B^2_\downarrow$ sublattice [see the green curve in Fig. 2(e)]. The $A^{1,2}$ sublattices do not show the dominating features, and the dominant $B^{1,2}$ sublattices are expected largely to determine the quantum modes of the magnetic LLs.

A uniform perpendicular electric field can drastically modify the electronic properties of bilayer silicene, mainly due to the destruction of the $z = 0$ mirror symmetry. The field also breaks down the spin-dependent state degeneracy and changes considerably the energy gap, leading to a dramatic transformation of the band structure. It is noticed that the effects due to an external electric field are revealed through the different Coulomb potentials on each sublattice, which depends on the atom heights. Such a field does not change either the geometric structure or the hopping integrals. Each conduction/valence band is split into a pair of energy subbands, as denoted by $S^c_{1,2}$ and $S^v_{1,2}$ in the inset of Fig. 2(a) for $E_z = 10$ mV/Å. The first and second conduction (valence) subbands are characterized, respectively, by the dominant $B^2_\downarrow$ and $B^1_\uparrow$ ($B^1_\downarrow$ and $B^2_\uparrow$) sublattices, for which the former is relatively close to the Fermi level. Such a feature will be magnified in the

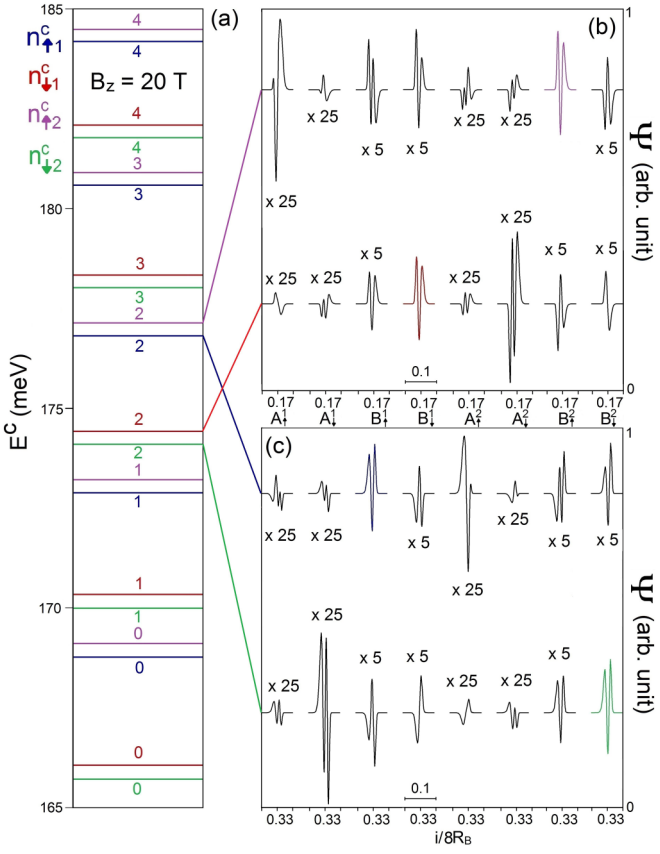

FIG. 3. At $B_z = 20$ T, the low-lying conduction LL energies (a); the spatial amplitude distributions for the $B^2_\uparrow$- and $B^1_\downarrow$-dominated LLs (b) and the $B^1_\uparrow$- and $B^2_\downarrow$-dominated LLs (c). The numbers in the abscissa represent the quantum numbers of those Landau levels. They are determined by the number of zero points of the spatial distributions on the dominating sublattices.

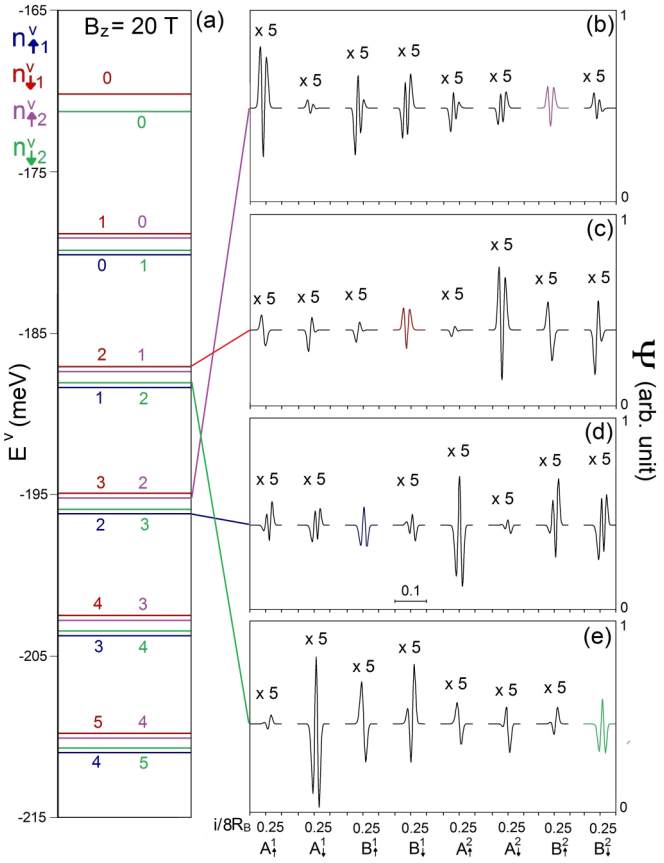

FIG. 4. At $B_z = 20$ T, the low-energy valence LLs (a); the spatial wave functions for the (b) $B^2_\uparrow$-, (c) $B^1_\downarrow$-, (d) $B^1_\uparrow$-, and (e) $B^2_\downarrow$-dominated LLs.

E_z-enriched LL energy spectra, as discussed below. Moreover, the sizable band gap is easily tuned by the external electric field. With a further increase of the field strength, the S^c_1 and S^v_1 energy subbands will be pushed down to the Fermi level, while the opposite is true for the S^c_2 and S^v_2 ones. Apparently, the band gap is reduced and then vanishes beyond a critical field ($E_z = 106$ meV), and a semiconductor-semimetal transition occurs at higher electric fields. This makes bilayer silicene extremely useful for electronic device applications.

B. The quantized Landau levels

The low-lying LLs possess rich characteristics due to the buckled structure, strong interlayer atomic interactions, and sizable SOCs. All the LLs are degenerate in the reduced first Brillouin zone with $|k_x| \leqslant 2\pi/aR_B$ and $|k_y| \leqslant 2\pi/\sqrt{3}a$ (an area of $4\pi^2/\sqrt{3}a^2R_B$). The ($k_x = 0, k_y = 0$) magnetic state is sufficient for understanding the main behaviors of magnetic quantization. The conduction and valence LLs, corresponding to the magnetic quantization of their electronic states, respectively, near the **K** (or **K**′) and **T** points, are asymmetric with respect to $E_F = 0$ (Figs. 3 and 4). They are reduced to doubly degenerate under the broken equivalence of the (B^1, B^2) sublattices and spin-up and spin-down configurations. The nondegenerate conduction (valence) states are localized at 1/6 and 2/6 (1/4) of the expanded unit cell. One should note that the conduction (valence) LLs are degenerate at the (1/6 and 4/6) and (2/6 and 5/6) [(1/4 and 3/4)] localization centers [31].

As for the low-lying conduction LLs, there exist four nondegenerate states for a chosen quantum number, as illustrated by blue, red, green, and purple in Fig. 3(a) for $B_z = 20$ T. They are distinguished by LL wave functions based on the $3p_z$- and spin-dependent subenvelope functions on the separate sublattices. The spatial distributions are similar to the oscillation modes of a harmonic oscillator. For example, the $n = 2$ LLs acquire well-behaved spatial oscillations with two nodes in the dominant sublattices, in which the $B^2_\uparrow$- and $B^1_\downarrow$-dominated states (the $B^1_\uparrow$- and the $B^2_\downarrow$-dominated ones) correspond to the 1/6 (2/6) localization center by the purple and red curves in Fig. 3(b) [the blue and green curves in Fig. 3(c)]. In parallel with $B^1_\uparrow$, $B^1_\downarrow$, $B^2_\uparrow$, and $B^2_\downarrow$, the sublattice- and spin-dominated LLs could be classified into four subgroups: $n^c_{\uparrow 1}$, $n^c_{\downarrow 1}$, $n^c_{\uparrow 2}$, and $n^c_{\downarrow 2}$. Here, c and v represent the conduction and valence LLs, respectively; 1/2 is the dominating B_1/B_2 sublattice and $\uparrow$ ($\downarrow$) indicates the dominating spin-up (spin-down) state of the subgroup. With this notation, we find it convenient to show the critical mechanisms related to LLs, such as the inter-LL optical transition (Fig. 9) and the inter-LL Coulomb scattering [38]. Each LL subgroup exhibits normal ordering for increasing state energy, i.e., n^c increases with E^c. However,

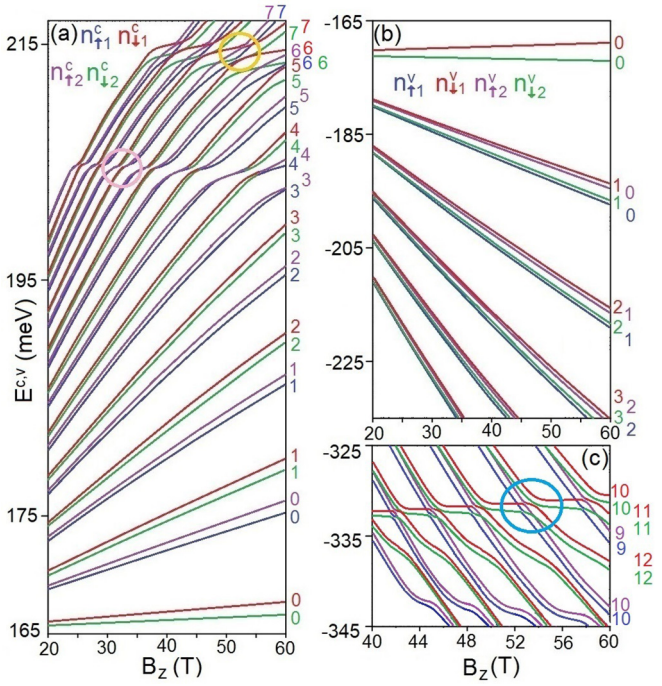

FIG. 5. The B_z-dependent LL energy spectrum: the blue, red, purple, and green curves are the different subgroups of conduction (a) and valence (b),(c) LLs based on the dominant $B^1_\uparrow$, $B^1_\downarrow$, $B^2_\uparrow$, and $B^2_\downarrow$ sublattices, respectively.

the LL energy spacing decreases with increasing n^c. There exists a very narrow energy spacing between the LLs at 1/6 (purple/red curve) and 2/6 (blue/green curve) centers under similar spin dominance, as seen from Fig. 3(a). For example, the sublattice-dependent energy splitting between $n^c_{\uparrow 2} = 0$ (1/6 center) and $n^c_{\uparrow 1} = 0$ (2/6 center) is only about 0.5 meV. This is much smaller than the spin-induced energy splitting, e.g., ∼3 meV for the $n^c_{\uparrow 1} = 0$ and $n^c_{\downarrow 1} = 0$ LLs (or $n^c_{\uparrow 2}$ and $n^c_{\downarrow 2}$ ones). The above-mentioned features also appear in the valence LLs, as clearly indicated in Figs. 4(a)–4(e). There are four valence LL subgroups, $n^v_{\uparrow 1}$, $n^v_{\downarrow 1}$, $n^v_{\uparrow 2}$, and $n^v_{\downarrow 2}$ [Fig. 4(a)]. The $B^1_\downarrow$-, $B^2_\downarrow$-, $B^2_\uparrow$-, and $B^1_\uparrow$-dominated LLs [Figs. 4(b)–4(e)] show the same 1/4 localization center. The nonequivalence of the B^1 and B^2 sublattices and the absence of spin-state degeneracy are responsible for these unique LLs.

The B_z-dependent LL energy spectrum, which is identified from the unique sublattice- and spin-dominated LL wave functions in bilayer AB-bt silicene, is critical in comprehending the diverse quantization phenomena. As for the conduction-LL energy spectrum, four distinct subgroups exhibit a similar magnetic field dependence, as clearly shown in Fig. 5(a). In the range of $165 \leqslant E^c \leqslant 195$ meV, the small-n^c LL energies have a monotonic/almost linear B_z dependence and the normal ordering among four subgroups. However, the abnormal behaviors, i.e., unusual field dependence and LL anticrossings, show up frequently at higher energies. The $n^c_{\uparrow 1}$ and $n^c_{\downarrow 2}$ LLs (blue and green curves) anticross with each other within a specific B_z range, and so do the $n^c_{\downarrow 1}$ and $n^c_{\uparrow 2}$ LLs (red and purple curves), as marked by the pink and yellow circles for the $n^c = 7$ LLs. Therefore, two kinds of intersubgroup anticrossings appear frequently for the specific quantum modes. These anticrossings clearly indicate that the wave functions of the perturbed LLs include the main and side modes, but not a single mode. Furthermore, such modes change substantially as the field strength is varied (discussed later with respect to Fig. 7) [24,31]. Similarly, there exists a simple relationship between the valence LL energies and the field strength for $-300 \leqslant E^v \leqslant -165$ meV. The deeper-energy spectrum presents two kinds of intersubgroup LL anticrossings arising from neighboring LLs, i.e., ($n^v_{\uparrow 1}$ *and* $n^v_{\downarrow 2} + 2$) [blue and green curves in Fig. 5(c)] and ($n^v_{\uparrow 2}$ *and* $n^v_{\downarrow 1} + 2$) (purple and red curves). Here, the $n^v = 10$ ($n^v = 12$) LLs acquire a side mode of 12 (10), leading to the anticrossings for ($n^v_{\uparrow 1} = 10$ and $n^v_{\downarrow 2} = 12$) and ($n^v_{\uparrow 2} = 10$ and $n^v_{\downarrow 1} = 12$) LLs, as indicated by the blue circle in Fig. 5(c). According to the Wigner–von Neuman noncrossing rule, two multimode (single-mode) LLs avoid crossing each other when they simultaneously possess certain identical modes (a nonidentical mode) with comparable amplitudes on the specific sublattices. The details of LL anticrossings have been shown in Figs. 3 and 4. The rich and unique LL energy spectra are closely related to the magnetic quantization of the unusual conduction and valence bands.

The rich sublattice- and spin-dominated LL energy spectra can be seen from the DOS, as shown in Figs. 6(a) and 6(b). Four subgroups of conduction and valence LLs are clearly displayed in the form of δ-function-like peaks. The low-energy DOS exhibits a uniform peak height in the presence of the same LL degeneracy and the absence of LL crossings. In each subgroup, the spacing between two neighboring peaks gradually decreases with increasing energy. Moreover, the subgroup-dependent DOS peaks appear under a specific ordering. The DOS of the conduction LLs presents the ordering of $n^c_{\downarrow 2}$-, $n^c_{\downarrow 1}$-, $n^c_{\uparrow 1}$-, and $n^c_{\uparrow 2}$-dominated peaks [green, red, blue, and purple in Fig. 6(a)], while the sequence for the DOS of the valence LLs is $n^v_{\downarrow 1}$-, $n^v_{\uparrow 2}$-, $n^v_{\downarrow 2}$-, and $n^v_{\uparrow 1}$-induced peaks [red, purple, green, and blue peaks in Fig. 6(b)], except for the $n^v_{\downarrow 1} = 0$ and $n^v_{\downarrow 2} = 0$ initial peaks. The well-behaved LL DOS peaks disappear at higher energy as a result of the frequent anticrossings/crossings [Figs. 5(a) and 5(c)].

The main features of the DOS peaks, covering the structure, height, number, and energy, could be verified by scanning tunneling spectroscopy (STS) [39–45]. To our knowledge, STS measurements have been successfully used to identify the magnetoelectronic energy for layered graphene. The LL energies in monolayer [39–41] and AB bilayer graphene [42,43] are confirmed with the square-root and linear dependence on B_z, respectively. The coexistence of $\sqrt{B_z}$ and linear B_z-dependent LL energies in ABA-stacked trilayer graphene [44], as well as the 3D and 2D characteristics of the Landau subbands in AB-stacked graphite [45], have also been examined. Moreover, the LL crossing and anticrossing phenomena can also be verified by measuring the shift of the plateaus in the quantum Hall effect (QHE) due to the increase in the LL degeneracy [46], while the latter can be examined by identifying the nonmonotonic changes in the structures, energies, intensities, and numbers of the DOS peaks [47]. Finally, the unusual magnetoelectronic properties in AB-bt bilayer silicene could be further verified by STS, including the normal and unusual B_z dependence, the sublattice- and spin-dominated four subgroups of LLs, as well as the special LL splittings, crossings, and anticrossings.

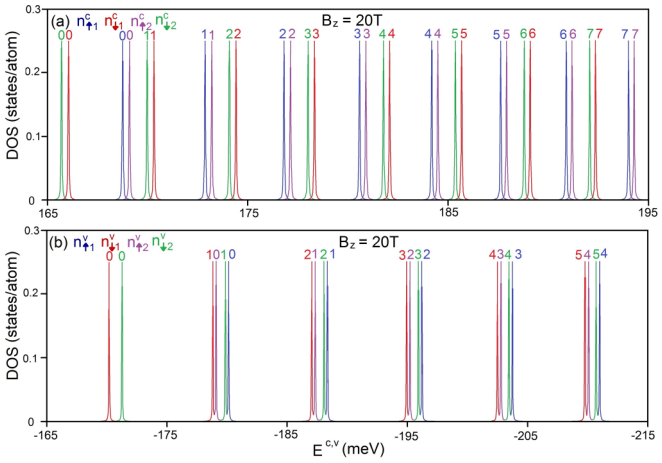

FIG. 6. The density of states of the conduction (a) and valence (b) LLs under a magnetic field of $B_z = 20$ T.

C. The electric-field-enriched Landau levels

The magnetoelectronic properties can be remarkably diversified by applying an external electric field. In the presence of composite electric and magnetic fields, the LL energies, which belong to ($n^{c,v}_{\uparrow 1}$ and $n^{c,v}_{\downarrow 1}$) along with ($n^{c,v}_{\uparrow 2}$ and $n^{c,v}_{\downarrow 2}$) subgroups, respectively, increase or decrease with the electric-field strength, as clearly shown in Figs. 7(a) and 8(a) by the blue and red curves and the purple and green curves. The E_z dependence of these subgroups is opposite for the B^1- and B^2-dominated LL energies. This clearly indicates E_z-enhanced sublattice nonequivalence by means of distinct Coulomb potential energies. There exist many LL anticrossings and crossings in the E_z-dependent energy spectra, in which the former are induced by the neighboring ($n^{c,v}_{\uparrow 1}$ and $n^{c,v}_{\downarrow 2}$) LLs (blue and green curves) and the ($n^{c,v}_{\downarrow 1}$ and $n^{c,v}_{\uparrow 2}$) ones (red and purple curves). However, such behaviors are absent between the $n^{c,v}_{\uparrow 1}$ and $n^{c,v}_{\downarrow 1}$ subgroups as well as between the $n^{c,v}_{\uparrow 2}$ and $n^{c,v}_{\downarrow 2}$ subgroups. That is, the spin-related LL energy spacing is weakly affected by E_z.

Here, the LL anticrossings are worthy of close examination. In the E_z-dependent energy spectrum, the intersubgroup anticrossings are only related to two neighboring LLs with a quantum number difference $\Delta n = 0, \pm 1, \pm 2$. These electronic transitions are either difficult to observe or changed to crossing behaviors. The conduction LLs anticross each other for ($n^c_{\downarrow,1}$ and $n^c_{\uparrow,2}$), ($n^c_{\downarrow,1}$ and $n^c_{\uparrow,2}+1$), as well as ($n^c_{\uparrow,1}$ and $n^c_{\downarrow,2}+1$), as shown in Fig. 7(a). The valence LLs behave similarly, as seen in Fig. 8(a). The $n^c_{\downarrow 1} = 1$ LL is chosen as an example for understanding the evolution of the wave functions as the field strength is increased [red curve in Fig. 7(b)]. In this case, the $n^c_{\downarrow 1} = 1$ LL has its first anticrossing with the $n^c_{\uparrow 2} = 1$ LL as E_z increases initially from zero (red and purple curves). They remain in their states for $n = 1$ on the $B^1_{\downarrow}$ and $B^2_{\uparrow}$ sublattices, as displayed in Fig. 7(c). However, one of two amplitudes (red) gives rise to phase switching during the anticrossing, e.g., those at $E_z = 0$ and 0.75 mV/Å. Moreover, the wave functions of the $n^c_{\downarrow 1} = 1$ and $n^c_{\uparrow 2} = 1$ LLs on the $B^2_{\uparrow}$ and $B^1_{\downarrow}$ sublattices, respectively, are greatly enhanced near the anticrossing center

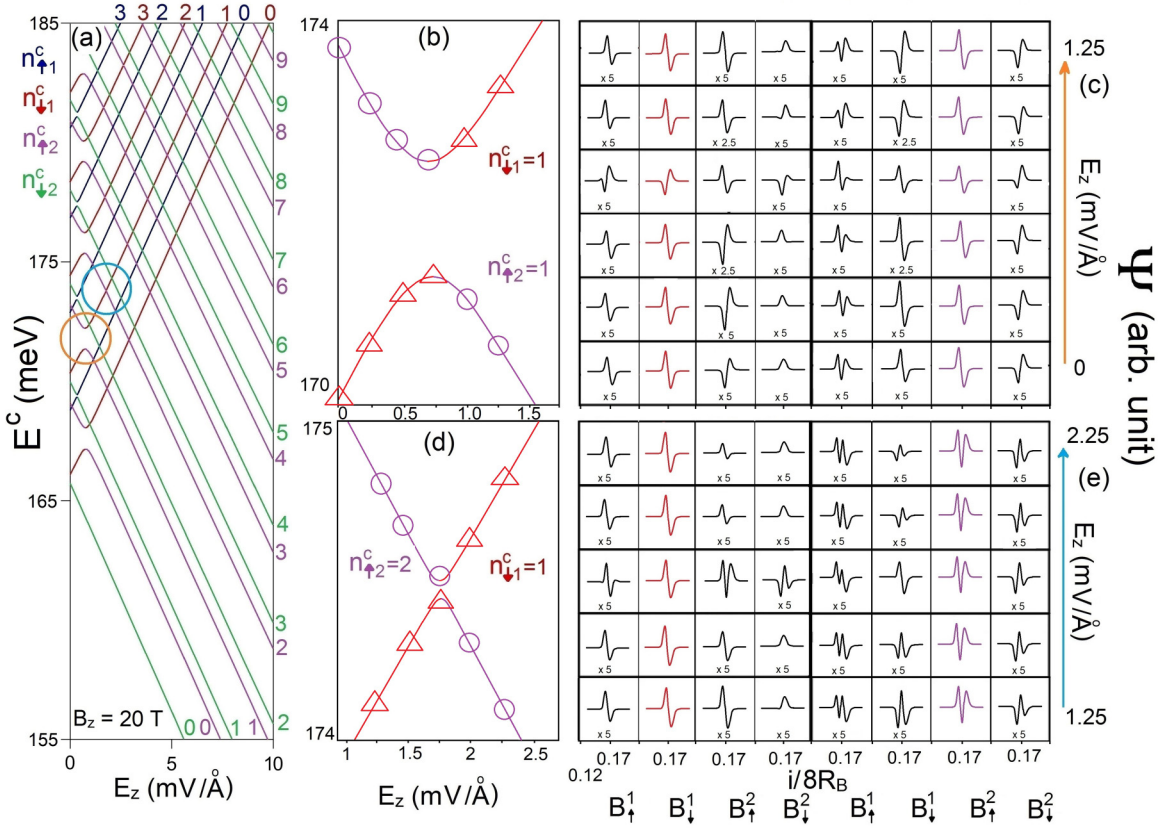

FIG. 7. The E_z-dependent conduction-LL energy spectrum (a) at $B_z = 20$ T; the ($n^c_{\downarrow 1} = 1$ and $n^c_{\uparrow 2} = 1$) and ($n^c_{\downarrow 1} = 1$ and $n^c_{\uparrow 2} = 2$) anticrossings (b), corresponding to the evolutions of wave functions in (c) and (e), respectively.

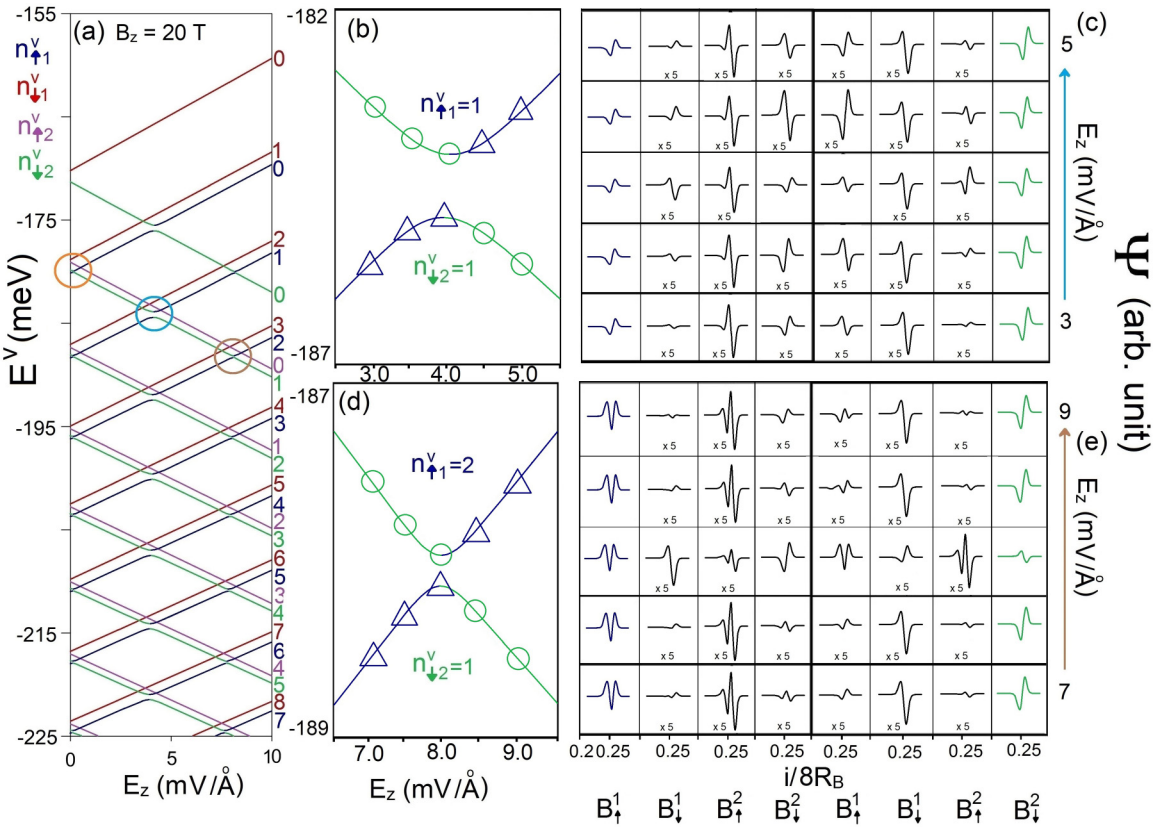

FIG. 8. The E_z-dependent valence-LL energy spectrum (a) at $B_z = 20$ T; the ($n^v_{\downarrow 2} = 1$ and $n^v_{\uparrow 1} = 1$) and ($n^v_{\downarrow 2} = 1$ and $n^v_{\uparrow 1} = 2$) anticrossings (b), corresponding to the evolutions of wave functions in (c) and (e), respectively.

and acquire comparable amplitudes commensurate with the dominating ones (right- and left-hand side black curves and by the red and purple curves). With a further increase of E_z, the $n^c_{\downarrow 1} = 1$ and $n^c_{\uparrow 2} = 2$ LLs encounter another weak anticrossing at $E_z \sim 1.75$ mV/Å in Fig. 7(d). In this case, the latter wave function on the $B^2_\uparrow$ sublattice is mapped directly onto the former wave function on the $B^2_\uparrow$ sublattice and vice versa in Fig. 7(e). The above-mentioned LL wave functions agree with the Wigner–von Neuman noncrossing rule. Similar anticrossings can be found for valence LLs in Fig. 8(a). For example, the $n^v_{\downarrow 2} = 1$ LL anticrosses with the $n^v_{\uparrow 1} = 1$ and $n^v_{\uparrow 1} = 2$ LLs at lower and higher electric fields in Figs. 8(b) and 8(d), respectively, as can be identified from the drastic changes of amplitude in Figs. 8(c) and 8(e) or even the transformation of oscillating modes on the $B^1_\uparrow$ and $B^2_\downarrow$ sublattices.

The AB-bt bilayer silicene sharply contrasts with AB-stacked bilayer graphene with respect to band structure and LLs. The former and latter, respectively, belong to an indirect-gap semiconductor and a semimetal. The graphene structure has two pairs of valence and conduction bands, with monotonic energy dispersions, a weak anisotropy, and a small overlap near the **K** point. Electronic states are independent of the spin configurations in the absence of SOCs. They remain doubly degenerate for the spin degree of freedom under any external fields. The neighboring states are magnetically quantized into well-behaved LLs with specific nodes in the oscillating probability distribution. For each (k_x, k_y) state, the LLs are eightfold-degenerate as a result of the equivalent sublattices and spin degeneracy. The conduction/valence LLs cannot be classified into four LL subgroups, in which they only present the regular B_z-dependent energy spectra without the anticrossing behaviors. Moreover, a perpendicular electric field can lead to a semimetal-semiconductor phase transition, but not the semiconductor-semimetal transition associated with the split energy bands. For silicene, the electric field also leads to a lifting of the degenerate **K** and **K**′ valleys for the magnetic LL states. There exist four degenerate LLs with frequent anticrossings in the E_z-dependent energy spectra. The important differences between bilayer silicene and graphene highlight the main features of the spin- and sublattice-dependent energy bands and LLs, demonstrating directly the distinct geometric structures, atomic interactions, and SOCs.

D. The optical conductivities

The feature-rich band structure and LLs are directly reflected in the unusual optical properties in bilayer silicene. The zero-field and magneto-optical conductivities are shown in Figs. 9(a) and 9(b). In the absence of external fields, the low-lying absorption spectrum mainly exhibits two kinds of special structures: discontinuities and logarithmic divergences [Fig. 9(a)]. There exist two shoulderlike structures at 0.42 and 0.48 eV and a sharp symmetric peak at 0.52 eV, which are, respectively, corresponding to the vertical transitions of extreme and saddle points in the energy-wave-vector space.

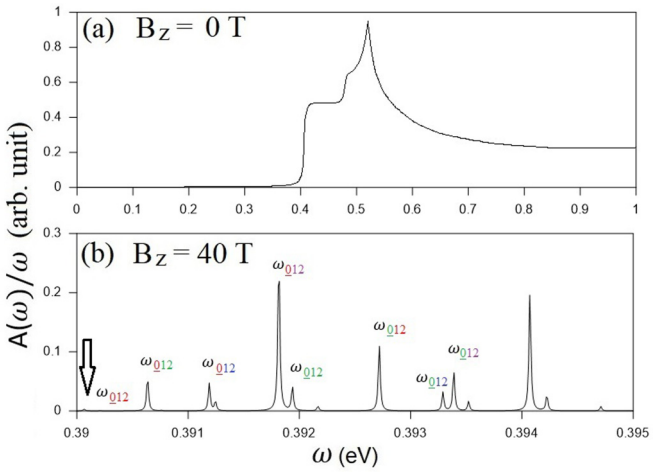

FIG. 9. The optical conductivities of AB-bt bilayer silicene under (a) zero magnetic field and (b) $B_z = 40$ T.

These optical structures can be verified by the infrared reflection spectroscopies and absorption spectroscopies [48,49].

The magnetoabsorption spectrum exhibits a lot of single, double, and twin nonuniform δ-function-like peaks [Fig. 9(b)]. Each symmetric peak is marked by ω_{n^v,n^c}, in which n^v and n^c indicate the quantum numbers of the unoccupied valence and the occupied conduction LLs, respectively. It is very difficult to identify the absorption peaks because they belong to the vertical transitions of the multimode LLs. Such transitions do not follow a specific selection rule. When a conduction/valence LL possesses a sufficiently large quantum number, its spatial distribution will be extended along the x axis so that it overlaps with that of the valence/conduction LL. This leads to the inter-LL optical transitions between those LLs. The intensities of absorption peaks depend strongly on the overlapping relation of the initial and final LLs. The threshold peak (optical gap), which is identified as $n^v_{1\downarrow} = 0 \rightarrow n^c_{1\downarrow} = 12$, is located at about 0.39 eV for $B_z = 40$ T [arrow in Fig. 9(b)]. This optical gap is much larger than the energy gap (0.3 eV) since the low-lying conduction and valence LLs are localized at different centers. As a result, the optical transitions among the low-lying conduction and valences LLs are forbidden. Moreover, the threshold peak frequency is relatively lower than that of the zero-field absorption spectrum. This is strong evidence of the anticrossing phenomena of the LLs quantized from the shoulderlike band structure. The former will be recovered to the latter when the phonon-assisted optical process is allowed at finite temperatures. In general, the optical gap is changed with the variation of the magnetic-field strength.

IV. CONCLUDING REMARKS

The magnetoelectronic and optical properties of bilayer AB-bt silicene are studied by the generalized tight-binding model combined with the dynamic Kubo formula and the gradient approximation. This system presents asymmetric conduction and valence bands about $E_F = 0$, parabolic and irregular energy dispersions, strong anisotropy, and an observable indirect gap, leading to rich and unique magnetic quantization. The low-lying conduction and valence LLs are doubly degenerate for each (k_x,k_y) state, in which they could be classified into four sublattice- and spin-dominated subgroups. The nonequivalence of B^1 and B^2 sublattices and spin splitting is clearly revealed in the field-dependent energy spectra. The LLs exhibit an almost linear B_z dependence near E_F, and there exists a specific ordering among the four subgroups. In general, the magnetic quantization phenomena in AB-bt bilayer silicene with complex SOCs and interlayer atomic interactions are very different from those of other 2D systems. The four sublattice- and spin-dominated groups of LLs in this system have not been revealed in other 2D emergent materials up to now. The STS measurements on LLs are very useful in examining the interplays of the complicated interlayer atomic interactions and the important SOCs. However, the abnormal energy spectra, accompanied by the frequent anticrossings and crossings, come to exist at higher/deeper energy. The unique features in bilayer silicene are expected to be verifiable by direct experimental measurements.

The electronic properties in bilayer silicene are very sensitive to an applied electric field. We can easily adjust the band gap, which is a crucial quantity for inducing a semiconductor-semimetal phase transition. Furthermore, the electric field also dramatically alters the main features of the LLs, including the spatial distribution and the anticrossing phenomena. The B^1- and B^2-dominated LL energies present the opposite E_z dependences, so that a lot of anticrossings and crossings appear at low field strength. The former, being associated with $\Delta n = 0$, ± 1, and ± 2, are identified from the drastic changes of wave-function amplitudes or even the mode transformation on the specific two sublattices. They mainly arise from the cooperation of the intrinsic interactions and the external fields. In short, the AB-stacked bilayer silicene and graphene are quite different from each other in band structure, LL degeneracy, field-dependent energy spectra, and anticrossing/crossing behaviors. We expect that the utilization of bilayer silicene will bring about a new opportunity in gate controlling of magnetoquantum channel conductance that can be applied to novel designs of Si-based nanoelectronics and nanodevices with enhanced mobilities.

AB-bt bilayer silicene exhibits unique and abnormal optical conductivities. In the absence of an external field, the absorption spectrum shows the shoulder structures and logarithmic divergence, which come, respectively, from the vertical transitions of the extreme and saddle points of the energy band. The magneto-optical peaks are enriched by the inter-LL excitations among four subgroups of LLs. Such transitions do not obey a specific optical selection rule, being in sharp contrast with those in bilayer graphene. They are very sensitive to the localization centers, and their intensities depend on the LL overlap. The absorption spectrum exhibits single-, double-, or twin-peak structures with nonuniform intensities. The main features of LLs are responsible for the unusual magneto-optical conductivities.

For the complicated band structure of bilayer silicene, the magnetic quantization can only be solved by the generalized tight-binding model. This is because the geometric symmetry, the intrinsic interactions (hopping integrals and SOCs), and the external fields need to be solved by the generalized tight-binding model simultaneously. On the other hand, using the

effective-mass model, it is very difficult or impossible to solve the magnetic quantization by the low-energy expansion because of distinct valleys, strong anisotropy, and weak energy dispersions in the conduction and valence bands. Even when the low-energy conduction **K** valley and the valence **T** valley enable the magnetic quantization to be solved, it is not exact enough to solve the quantization separately, which is inconsistent with the requirement of quantum statistics (the distribution of fermions).

The tight-binding model is capable of directly combining with single- and many-particle theories to explore other fundamental physical properties, such as magneto-optical properties, the quantum Hall effect, and magneto-Coulomb excitations. We have built up a theoretical framework to investigate the critical physical properties of condensed-matter systems. The optical conductivities are studied using the dynamic Kubo formula and the gradient approximation. The quantum Hall effect is explored using the static Kubo formula within the linear-response theory. Moreover, the random-phase approximation needs to be modified to agree with the layer-dependent tight-binding model, and then it is available for exploring magneto-electronic excitations in few-layer silicene systems. That is, intra- and interlayer atomic interactions and intra- and interlayer Coulomb interactions are taken into account simultaneously. The whole theoretical framework is very concise and meaningful.

ACKNOWLEDGMENTS

This material is based upon work supported by the Air Force Office of Scientific Research under award number FA2386-18-1-0120. We would also like to acknowledge the financial support from the Ministry of Science and Technology of the Republic of China (Taiwan) under Grant No. 105-2112-M-017-002-MY2.

[1] C. H. Lui, L. M. Malard, S. H. Kim, G. Lantz, F. E. Laverge, R. Saito *et al.*, Nano Lett. **12**, 5539 (2012).
[2] T. N. Do, C. Y. Lin, Y. P. Lin, P. H. Shih, and M. F. Lin, Carbon **94**, 619 (2015).
[3] P. Vogt, P. De Padova, C. Quaresima, J. Avila, E. Frantzeskakis, M. C. Asensio, A. Resta, B. Ealet, and G. L. Lay, Phys. Rev. Lett. **108**, 155501 (2012).
[4] T. Li, C. Eugenio, C. Daniele, G. Carlo, F. Marco, D. Madan *et al.*, Nat. Nanotech. **10**, 227 (2015).
[5] B. Mohan, A. Kumar, and P. K. Ahluwalia, Physica E **53**, 233 (2013).
[6] H. S. Liu, N. Han, and J. J. Zhao, J. Phys.: Condens. Matter **26**, 475303 (2014).
[7] J. J. Liu and W. Q. Zhang, RSC Adv. **3**, 21943 (2013).
[8] F. Liu, C.-C. Liu, K. Wu, F. Yang, and Y. Yao, Phys. Rev. Lett. **111**, 066804 (2013).
[9] J. E. Padilha and R. B. Pontes, J. Phys. Chem. C **119**, 3818 (2015).
[10] X. Q. Wang and Z. G. Wu, Phys. Chem. Chem. Phys. **19**, 2148 (2017).
[11] Y. P. Lin, C. Y. Lin, Y. H. Ho, T. N. Do, and M. F. Lin, Phys. Chem. Chem. Phys. **17**, 15921 (2015).
[12] H. X. Fu, J. Zhang, Z. J. Ding, H. Li, and S. Menga, Appl. Phys. Lett. **104**, 131904 (2014).
[13] J. Y. Wu, C. Y. Lin, G. Gumbs, and M. F. Lin, R. Soc. Chem. Adv. **5**, 51912 (2015).
[14] A. Iurov, G. Gumbs, and D. H. Huang, J. Mod. Opt. **64**, 913-920 (2016).
[15] H. X. Da, W. Q. Ding, and X. H. Yan, Appl. Phys. Lett. **110**, 141105 (2017).
[16] R. Yaokawa, T. Ohsuna, T. Morishita, Y. Hayasaka, M. J. S. Spencer, and H. Nakano, Nat. Commun. **7**, 10657 (2016).
[17] A. Iurov, G. Gumbs, and D. H. Huang, J. Phys.: Condens. Matter **29**, 135602 (2017).
[18] P. H. Shih, Y. H. Chiu, J. Y. Wu, F. L. Shyu, and M. F. Lin, Sci. Rep. **7**, 40600 (2017).
[19] F. F. Zhu, W. J. Chen, Y. Xu, C. L. Gao, D. D. Guan, C. H. Liu, D. Qian, S. C. Zhang, and J. F. Jia, Nat. Mater. **14**, 1020 (2015).
[20] S.-C. Chen, C.-L. Wu, J.-Y. Wu, and M.-F. Lin, Phys. Rev. B **94**, 045410 (2016).
[21] J.-Y. Wu, S.-C. Chen, G. Gumbs, and M.-F. Lin, Phys. Rev. B **95**, 115411 (2017).
[22] O. L. Berman, G. Gumbs, and R. Y. Kezerashvili, Phys. Rev. B **96**, 014505 (2017).
[23] C. J. Tabert and E. J. Nicol, Phys. Rev. B **88**, 085434 (2013).
[24] C. Y. Lin, J. Y. Wu, Y. J. Ou, Y. H. Chiu, and M. F. Lin, Phys. Chem. Chem. Phys. **17**, 26008 (2015).
[25] Y. C. Huang, C. P. Chang, and M. F. Lin, Nanotechnol. **18**, 495401 (2007).
[26] Y. H. Ho, W. P. Su, and M. F. Lin, R. Soc. Chem. Adv. **5**, 20858 (2015).
[27] C. Kamal, A. Chakrabarti, A. Banerjee, and S. K. Deb, J. Phys.: Condens. Matter **25**, 085508 (2013).
[28] Y. Zhang, T.-T. Tang, C. Girit, Z. Hao, M. C. Martin, A. Zettl, M. F. Crommie, Y. R. Shen, and F. Wang, Nature (London) **459**, 820 (2009).
[29] J. B. Oostinga, H. B. Heersche, X. Liu, A. F. Morpurgo, and L. M. K. Vandersypen, Nat. Mater. **7**, 151 (2007).
[30] C.-C. Liu, H. Jiang, and Y. Yao, Phys. Rev. B **84**, 195430 (2011).
[31] Y. K. Huang, S. C. Chen, Y. H. Ho, C. Y. Lin, and M. F. Lin, Sci. Rep. **4**, 7509 (2014).
[32] M. F. Lin and K. W.-K Shung, Phys. Rev. B **50**, 17744(R) (1994).
[33] C. Y. Lin, T. N. Do, Y. K. Huang, and M. F. Lin, IOP E-book (2017).
[34] M. Koshino, H. Aoki, K. Kuroki, S. Kagoshima, and T. Osada, Phys. Rev. Lett. **86**, 1062 (2001).
[35] M. Taut, H. Eschrig, and M. Richter, Phys. Rev. B **72**, 165304 (2005).
[36] D. R. Hofstadter, Phys. Rev. B **14**, 2239 (1976).
[37] M. Kohmoto, Ann. Phys. (NY) **160**, 343 (1985).
[38] J.-Y. Wu, S.-C. Chen, O. Roslyak, G. Gumbs, and M.-F. Lin, ACS Nano **5**, 1026 (2011).
[39] G. Li, A. Luican, and E. Y. Andrei, Phys. Rev. Lett. **102**, 176804 (2009).
[40] Y. J. Song, A. F. Otte, Y. Kuk, Y. K. Hu, D. B. Torrance, P. N. First *et al.*, Nature (London) **467**, 185 (2010).

[41] W.-X. Wang, L.-J. Yin, J.-B. Qiao, T. Cai, S.-Y. Li, R.-F. Dou, J.-C. Nie, X. Wu, and L. He, Phys. Rev. B **92**, 165420 (2015).
[42] G. M. Rutter, S. Jung, N. N. Klimov, D. B. Newell, N. B. Zhitenev, and J. A. Stroscio, Nat. Phys. **7**, 649 (2011).
[43] L.-J. Yin, Y. Zhang, J.-B. Qiao, S.-Y. Li, and L. He, Phys. Rev. B **93**, 125422 (2016).
[44] L.-J. Yin, S.-Y. Li, J.-B. Qiao, J.-C. Nie, and L. He, Phys. Rev. B **91**, 115405 (2015).
[45] G. H. Li and E. Y. Andrei, Nat. Phys. **3**, 623 (2007).
[46] T. Taychatanapat, K. Watanabe, T. Taniguchi, and P. Jarillo-Herrero, Nat. Phys. **7**, 621 (2011).
[47] K. F. Mak, J. Shan, and T. F. Heinz, Phys. Rev. Lett **104**, 176404 (2010).
[48] Z. Q. Li, E. A. Henriksen, Z. Jiang, Z. Hao, M. C. Martin, and P. Kim *et al.*, Nat. Phys. **4**, 532 (2008).
[49] L. M. Zhang, Z. Q. Li, D. N. Basov, M. M. Fogler, Z. Hao, and M. C. Martin, Phys. Rev. B **78**, 235408 (2008).